SCIENTIFIC REPORTS

OPEN

Received: 14 September 2017
Accepted: 28 December 2017
Published online: 18 January 2018

Preparation of polyaniline/PbS core-shell nano/microcomposite and its application for photocatalytic H_2 electrogeneration from H_2O

Mohamed Rabia[1,2], H. S. H. Mohamed[3], Mohamed Shaban[1] & S. Taha[3]

Lead sulfide (PbS) and polyaniline (PANI) nano/microparticles were prepared. Then, PANI/PbS core-shell nano/microcomposites (I, II, and III) were prepared by oxidative polymerization of different aniline concentrations (0.01, 0.03, and 0.05 M), respectively, in the presence of 0.05 M PbS. FT-IR, XRD, SEM, HR-TEM, and UV-Vis analyses were carried out to characterize the samples. From the FT-IR data, there are redshifts in PbS and PANI nano/microparticles bands in comparison with PANI/PbS nano/microcomposites. The average crystallite sizes of PANI/PbS core-shell nano/microcomposites (I, II, and III) from XRD analyses were 46.5, 55, and 42.16 nm, respectively. From the optical analyses, nano/microcomposite (II) has the optimum optical properties with two band gaps values of 1.41 and 2.79 eV. Then, the nano/microcomposite (II) membrane electrode supported on ITO glass was prepared and applied on the photoelectrochemical (PEC) H_2 generation from H_2O. The characteristics current-voltage and current-time behaviors were measured at different wavelengths from 390 to 636 nm. Also, the incident photon-to-current conversion efficiency (IPCE) under monochromatic illumination condition was calculated. The optimum values for IPCE were 36.5 and 35.2% at 390 and 405 nm, respectively. Finally, a simple mechanism for PEC H_2 generation from H_2O using the nano/microcomposite (II) membrane electrode was mentioned.

The economic model and the present global society are the most critical challenges that can be confronted the world in 21st for the provision of clean and renewable energy to satisfy the increasing human demands. Renewable and cleaning energy can be offered by sunlight[1]. In this context, hydrogen (H_2) is considered as the cleanest and environmentally friendly energy; it has an ideal fuel for the future. Photoelectrochemical (PEC) H_2 generation can be occurred by water splitting with semiconductor materials. This technique is the most straightforward conversion because only water and sunlight can produce H_2 and the combustion process in hydrogen fuel cells leads to electricity with water as the only by-product[2,3].

In recent years, H_2 has become a hot academic topic since Fujishima and Honda were the first who worked in photocatalytic water splitting using a TiO_2 electrode[4]. These advances have motivated the search for a growing list of applications of the functional materials[5–7]. Among these materials, metal sulfide semiconductors (SCs) have attracted broad interest in photocatalysis and solar cell applications because of their tunable band gap and unique optical properties[8–11]. In particular, lead sulfide (PbS) is one of the metal sulfides which has promising photosensitive properties and can be prepared as n or p-type for solar energy applications due to the variety of band gaps that affected by the particle sizes[12,13]. Moreover, the absorption capacity of PbS nanomaterials in many regions of the light and can reach to the infrared region in wavelengths ~800–1700 nm, with a percent of about 40% of the solar radiation on the earth's surface. So PbS nanoparticles could improve light absorption very much[14]. The metals sulfides SCs can be prepared by several techniques such as thermal evaporation, spray deposition, and chemical

[1]Nanophotonics and Applications Lab, Physics Department, Faculty of Science, Beni-Suef University, Beni-Suef, 62514, Egypt. [2]Polymer Research Laboratory, Chemistry Department, Faculty of Science, Beni-Suef University, Beni-Suef, 62514, Egypt. [3]Physics Department, Faculty of Science, Fayoum University, EL-Fayoum, Egypt. Correspondence and requests for materials should be addressed to M.S. (email: mssfadel@aucegypt.edu)

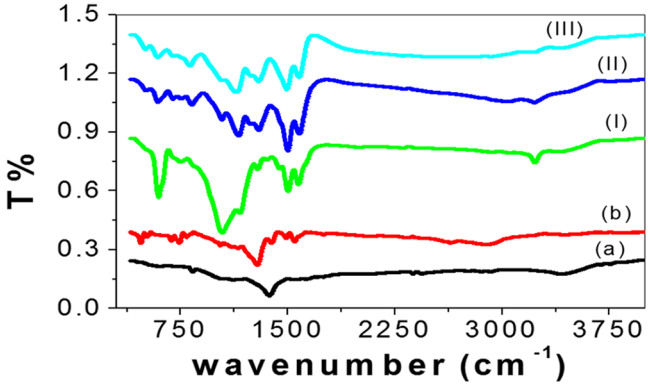

Figure 1. FTIR analyses of (**a**) PbS and (**b**) PANI nano/microparticles, and PANI/PbS core-shell nano/microcomposites (I, II, and III).

bath deposition (CBD). CBD is the most widely used method due to its simplicity and low-cost effectiveness, and it can occur at low temperature[15].

In addition, there are some studies depended on PbS materials in photocatalytic water splitting for solar hydrogen generation. Chih-Hsiung *et al*. showed decoration of PbS nanoparticles on Al-doped ZnO nanorod array thin film as a photoelectrode for solar water splitting leading a maximum photocurrent density of 1.65 mW cm^{-2} [16]. The study carried out from solution contained 0.25 M Na_2S and 0.35 M Na_2SO_3 at pH = 13 using 350 W Xe lamp. Hernandez-Borja *et al*. prepared PbS/CdS by CBD process and applied it as photoelectrode with an efficiency of 1.63% for solar energy applications[17]. Cui *et al*. synthesized PbS intercalated $K_2La_2Ti_3O_{10}$, by ion-exchange reaction under the microwave irradiation. But the amount of H_2 generated was small of about 127 mmol/g after 3 h irradiation of ultraviolet light[18].

Moreover, the enormous progress in the synthesis of the composite core-shell structures has significantly advanced research ability to tune their optical, electrical, mechanical, and chemical properties for using them in new photo/electro-applications[19]. On the other hand, a significant interest among researchers has been aroused to conducting polymers due to their curious electronic, high conductivity, magnetic and optical properties, high stability, simple preparations, and good environmental compatibility[20–22]. Because of these useful properties, the photoactivity can be enhanced by using PANI as a photosensitizer to modify the photocatalysts[23]. The presence of conjugated π electrons along the backbone of polymer like PANI provides the ability to support positive as well as negative charge carriers. Exciting and unique physical properties are expected when the delocalized carrier sinter acts with the semiconductor quantum dots with high mobility along the chain. There were variously modified photocatalysts based on PANI such as PANI/TiO_2[24], PANI/$BiVO_4$[23], PANI/SnO_2[25], and PANI/MoO_3[26]. Wang *et al*. have designed and synthesized monodisperse PANI@CdS core-shell nanospheres to probe the mechanisms of photocorrosion inhibition and photocatalytic H_2 production[27]. Zhang *et al*. revealed that the exciting enhanced visible light photocatalytic activity and excellent anti-photocorrosion performance of CdS photocatalysts were obtained after hybridized by monolayer PANI[28].

The efficiency of PEC H_2 production using these composites still limited and the designed nanocomposites efficiency need more enhancement[27,29]. Moreover, many studies used high-cost techniques and depended on chemical substances such as CH_3COOH, HCL, HNO_3, and H_2SO_4 as a source for H_2[30]. So the critical issues for H_2 generation process are to be commercially available, reducing the synthesis and applications cost, and enhance the stability of the used photocatalysts[31–34].

In this work, the synthesis of PbS and PANI nano/microparticles, and PANI/PbS core-shell nano/microcomposites (I, II, and III) using simple and low-cost techniques was carried out. Moreover, the structural, morphological, and optical properties of the fabricated nanostructures were investigated using different characterization techniques. Also, the effect of aniline concentrations on the properties of the fabricated nano/microcomposites was studied. Moreover, PEC water splitting properties and efficiencies such as I-V and I-T responses were studied on PANI/PbS/ITO core-shell nano/microcomposite (II) membrane electrode. Also, IPCE under monochromatic illumination conditions was addressed.

Results and Discussion

Nano/microparticles characterization. It is known that the surface structures of the PANI, PbS, and PANI/PbS core-shell nano/micromaterials influence their optical properties, for this reason, it was imperative to investigate their structures and morphologies. The structural analyses of all nano/microparticles were examined, in which the FT-IR spectra are shown in Fig. 1. In addition, the data of these nano/microparticles are mentioned in Table 1. From the figure and table, there are redshifts of bands of PbS (a) and PANI (b) nano/microparticles in comparison with that observed for the PANI/PbS nano/microcomposites (I, II, and III). This appears in the frequencies of the heteropolar diatomic molecule in PbS and N–H stretching vibrations of amino groups in PANI. These shifting may result from the increased energy of interaction between PbS and PANI levels. While a little blue-shift in bands in all core-shell nano/microcomposites (I, II, III) with increasing the PANI ratio in the composite from I to III. These shifts are a result of the interaction between the constituents of the formed nano/microcomposites[35].

Band position (cm^{-1})					
PANI/PbS composite I	PANI/PbS composite II	PANI/PbS composite III	PbS	PANI	Assignment
3229	3226	3221	—	3401	N–H stretching vibrations of amino groups in the nano/microcomposite[58]
2925	2922	2920	—	2918	Vibration of C-H aromatic ring
1501	1500	1492	—	1530	The coordinated water molecule and C = C stretching vibrations of quinoid ring[59]
1289	1295	1295	1357	—	The frequencies of heteropolar diatomic molecules of lead sulfide[60]
1301	1301	1300	—	1301	C = C vibration of benzoid rings
1165	1155	1137	—	1138	C–N stretching vibrations
1041	1039	1040	1061	—	The frequencies of heteropolar diatomic molecules of lead sulide[60]
747	827	814	—	798	The aromatic C—H out-plane bending
596	592	590	—	587	Para disubstituted aromatic rings[61]

Table 1. The FTIR analyses of the PbS, PANI, and PANI/PbS nano/microcomposites (I, II, and III).

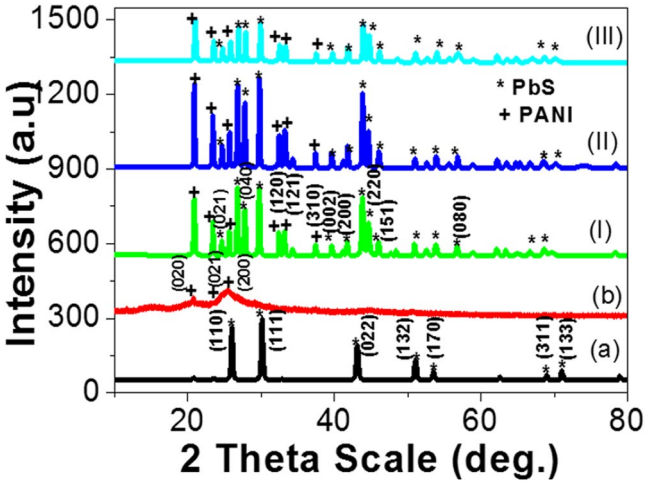

Figure 2. X-ray analyses of (**a**) PbS and (**b**) PANI nano/microparticles, and PANI/PbS core-shell nano/microcomposites (I, II, and III).

The X-ray diffractometers at room temperature for PbS and PANI nano/microparticles, and PANI/PbS core-shell nano/microcomposites (I, II, and III) are shown in Fig. 2. The X-ray analysis of PbS particles is shown in Fig. 2(a). There are seven distinct crystalline peaks appeared centered at 2θ = 25.98°, 30.17°, 43.12°, 51.14°, 53.70°, 68.82°, and 71.01° corresponding to (110), (111), (022), (132), (170), (311), and (133), respectively. The average crystallite size of the PbS particles is determined using the full width at half maximum (W) data. The determination process takes place using Scherrer's formula[35] D = 0.9λ/W cosθ; where W is in radians, θ is the Bragg's angle, λ is the X-ray wavelength (CuKα = 0.15405 nm). From the calculation process data, the average crystallite size of the PbS particles is ~36.3 nm.

The XRD patterns of PANI particles is illustrated in Fig. 2(b). The XRD spectrum of PANI clearly indicated the preparation of PANI crystallites with crystalline domains. Three distinct crystalline peaks appeared centered at 2θ = 15.18°, 21.12°, and 25.49°, which corresponding to (020), (021), and (200) crystal planes, respectively, of PANI in its emeraldine salt form[36]. The characteristic peaks at 2θ = 15.18° and 25.49° are ascribed to the perpendicular and parallel periodicity of the polymer chain, respectively[37,38]. The average size of the PANI crystallites is determined from the full width at half maximum (W) in radians using Scherrer's formula; D = 0.9λ/W cos θ; where λ is the X-ray wavelength (CuKα = 0.15405 nm)[35]. The calculated value of the average crystallite size of the PANI is ~100 nm.

The XRD patterns of PANI/PbS core-shell nano/microcomposites (I, II, and III) appear in Fig. 2 (I–III). From the figure, the formation of crystalline Six distinct crystalline peaks appeared centered at 2θ = 15.18°, 21.12°, 25.49°, 32.4°, 33.1°, and 41,8° corresponding to (020), (021), (200), (120), (121), and (310), respectively, for crystal planes of PANI in its emeraldine salt form[39]. In addition, the two characteristic peaks at 2θ = 15.18°, 23.2° are ascribed to the perpendicular and parallel periodicity of the polymer chain, respectively[40]. Moreover, there are 14 distinct crystalline peaks for PbS core nanoparticles appeared centered at 2θ = 24.4°, 25.98°, 27.7°, 30.17°, 39.6°, 41.8°, 43.12°, 44.3°, 45.9°, 51.14°, 53.70°, 68.82°, and 71.01° corresponding to (021), (110), (200), (111), (002), (200), (022), (220), (151), (132), (170), (311), and (133). The average crystallite sizes of the PANI/PbS core-shell nano/microcomposites (I, II, and III) are determined from the full width at half maximum (W) data. From the calculation process data, the average crystal sizes of the PANI/PbS core-shell nano/microcomposites (I, II, and III) are 46.5, 55, and 42.16 nm, respectively. The increasing in size with aniline concentrations from 0.01 M (composite I) to 0.03 M (composite II) is due to increasing of the nucleation sites that cause more coalescence of the

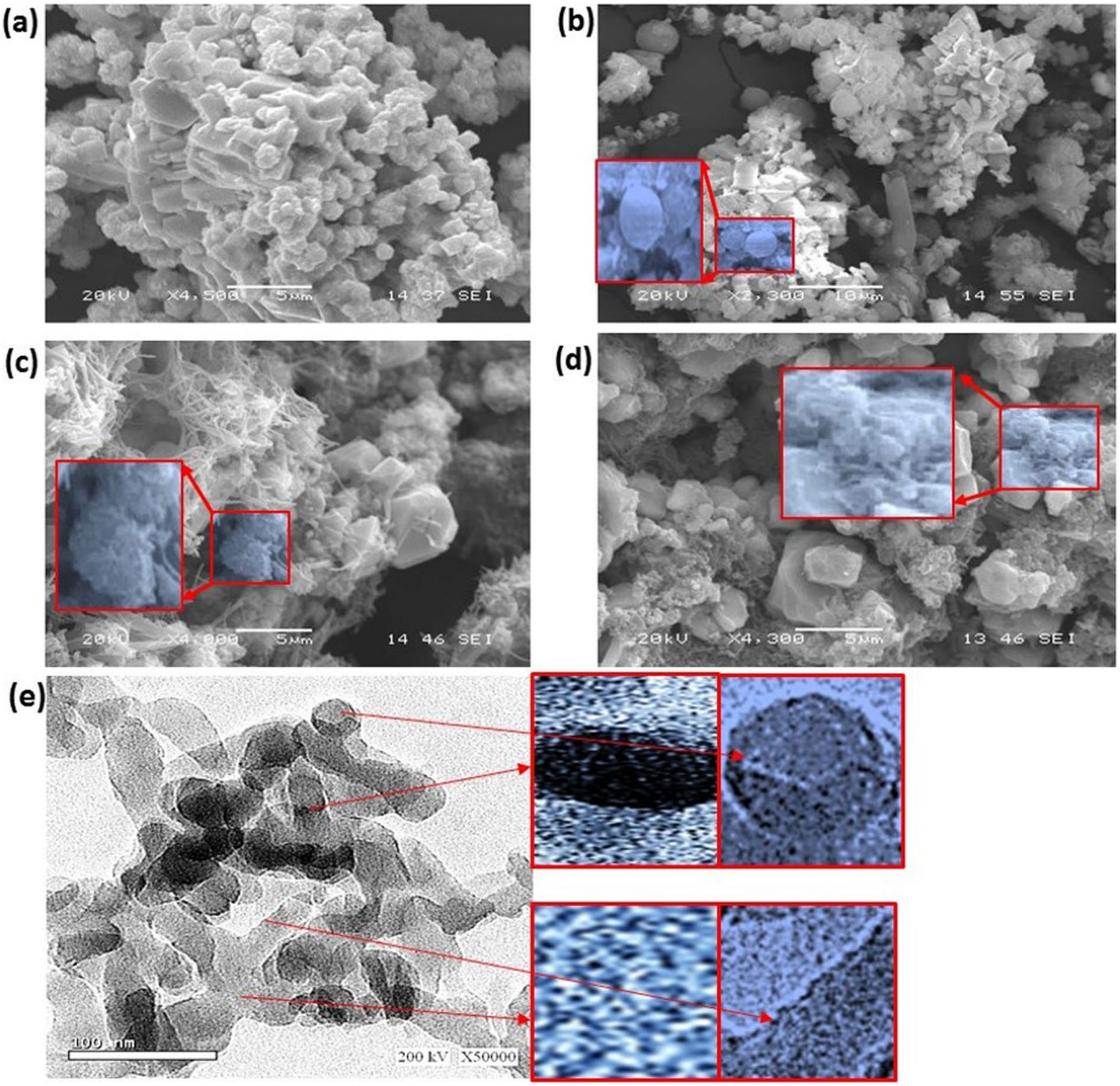

Figure 3. SEM analyses of (**a**) PbS nanoparticles and (**b–d**) PANI/PbS core-shell nano/microcomposites (I, II, and III). (**e**) HR-TEM of PANI/PbS core-shell nano/microcomposite (II).

deposited nano/microcomposite[41]. But with further increasing of the aniline concentration to 0.05 M (composite III), the particles sizes decrease due to the reduction of the Vander Waals force interactions that exist between the crystals because of disorder the particles deposition during the formation of core-shell composite[42].

The morphology of the PbS nanoparticles is investigated by SEM analyses as shown in Fig. 3(a). This image clearly illustrates the formation of spherical and ribbed nanoparticles with an average particle size of 100 nm. Moreover, SEM for PANI/PbS core-shell nano/microcomposites (I, II, and III) are shown in Fig. 3(b to d), respectively, From the figure, the formation of nano/microcomposites with spherical, ribbed, and fiber shapes are formed with average particles sizes of 250 nm. Moreover, with increasing of the aniline concentration during the preparation of core-shell nano/microcomposites, the fibers shapes increase as shown in the insets of Fig. 3(b–d).

The TEM analysis of PANI/PbS core-shell nano/microcomposite (II) is shown in Fig. 3(e). From the figure, the PbS nanoparticles (black color) are embedded in PANI (gray color) indicates the formation of PANI/PbS core-shell nano/microcomposite. The spherical and ribbed shapes of PbS nanoparticles appear clearly in the magnified parts of Fig. 3(e) (top insets). In addition, the nanoporous nature of PANI shell appears in the magnified parts of Fig. 3(e) (bottom insets). The estimated shell thickness is about 15–35 nm.

The study of optical properties of the PANI and PbS nano/microparticles, and PANI/PbS core-shell nano/microcomposites (I, II, and III) is one of the essential factors to extend their applications. The optical absorbance spectra PANI, PbS nano/microparticles and the composites with different aniline concentration values are represented in Fig. 4(A).

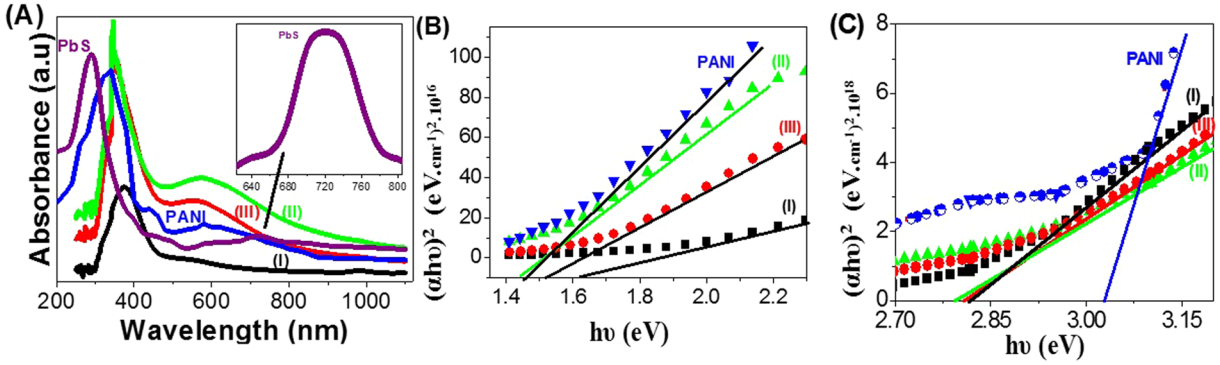

Figure 4. (**A**) Optical absorbance analyses and (**B**,**C**) band-gap values of PbS and PANI nano/microparticles, and PANI/PbS core-shell nano/microcomposites (I, II, and III).

In the case of PANI nano/microparticles (green line), the spectrum shows strong absorption peak centered at 333 nm in the UV-region, and two broad peaks at 439 and 600 nm in the visible region. The sharp peak is due to Π-Π* transitions from the benzenoid ring[43], whereas the two broad peaks in the visible region are due to high conjugation of the aromatic polymer chain[44]. While, in the case of PbS nanoparticles, the spectrum shows the presence of a sharp peak at UV region at ~290 nm and another small broad one at 720 nm near-IR region (inset of Fig. 4(A)) attributed to intrinsic band-gap absorption of PbS and structural defect absorption, respectively[45].

In addition, in the case of PANI/PbS core-shell nano/microcomposites (I, II, and III), the spectra show strong absorption peak centered at 360 nm in the UV-region and another broad peak at 570 nm in the visible region. From the figure, the formation of PANI/PbS nano/microcomposites makes an enhancement of the absorbance values especially in the UV and visible regions. This absorbance increases with the increase of the aniline concentrations in the composites from 0.01 to 0.03 M (composite (II)), then decrease with further increasing of aniline concentration to 0.05 M.

Based on direct allowed transition type the optical band gap of powder samples can be estimated using Tauc's equation (Eq. 1)[46].

$$\alpha = (h\nu - E_g)^{1/2}/h\nu \quad (1)$$

where α is the absorption coefficient, A is the absorbance of the sample, E_g is the optical band gap, h is the Planck constant, and ν is reciprocal of the wavelength. α is given by Eq. (2)[47,48].

$$\alpha = 2.303\ x\ 10^3 A\beta/lC \quad (2)$$

where β is the density of PANI (1.36 g/cm^3) and PANI/PbS core-shell nano/microcomposites (3.2 to 3.6 g/cm^3), $l = 1.0$ cm = the path of the quartz cell, and C is the concentration of the powder in the suspension.

The band gaps values for PANI nano/microparticles and PANI/PbS core-shell nano/microcomposites (I, II, and III) with different aniline concentrations are estimated by extrapolation of the straight line of the plot of $(\alpha h\upsilon)^2$ versus $h\upsilon$, as shown in Fig. 4(B,C). PANI has two band gaps at 1.45 and 3.03 eV; this is matched with the previous study of Shaban *et al.*[47]. Also, each nano/microcomposite has two band gaps. The first band gaps values, Fig. 4(B), are 1.62, 1.41, and 1.52 eV for nano/microcomposites (I, II, and III), respectively. In which the values of band gaps decrease with increasing of the aniline concentrations in the nano/microcomposites from 0.01 to 0.03 M, then increase with the further increase of the aniline concentration to 0.05 M. In addition, the second band gaps are represented in Fig. 4(C). From the figure, the band gaps values have the same behavior of the first values, in which they decrease with the increase of the aniline concentrations in the nano/microcomposites (I, II, and III) and have values of 2.82, 2.79, and 2.81 eV, respectively. Moreover, the band gap of PbS nanocrystallites is calculated from Fig. S1 (Supplementary data). This figure shows two band gap values at 1.93 and 3.11 eV corresponding to the two absorption band that observed in the optical spectrum of PbS, Fig. 4(A). From the obtained band gap values of PbS, PANI, and PANI/PbS core-shell nano/microcomposites (I, II, and III), the enhancement in the optical properties of the composites is due to the significant effect of the synergistic interaction of PbS and PANI matrix[49], this is confirmed by the FT-IR shift peaks and X-ray analyses. Moreover, the values of the band gaps clearly refer to the enhancement of the optical properties of the nano/microcomposites (I, II, and III), in which nano/microcomposite (II) has the optimum values that qualify it for application in H_2 generation systems.

Photoelectrochemical H_2 generation. The photoelectrochemical (PEC) behaviors of the PANI/PbS/ITO nanocomposite (II) membrane electrodes supported on ITO glass was measured in dark and light without optical filters as shown in Fig. 5. The PEC behaviors were measured under illumination of 400 W metal-halide Lamp in 100 ml of 0.3 M $Na_2S_2O_3$ solution at room temperature (25 °C) with a sweep rate of 1 mV/s. The prepared electrode with 1 cm^2 surface area is used as the photoanode, and Pt-electrode of the same area is used as the counter electrode. Upon exposure to light, the large surface area of the nano/microcomposite electrode will produce a high density of electron-hole pairs, which will motivate the splitting of H_2O molecules under the effect of light to carry out the hydrogen generation reaction.

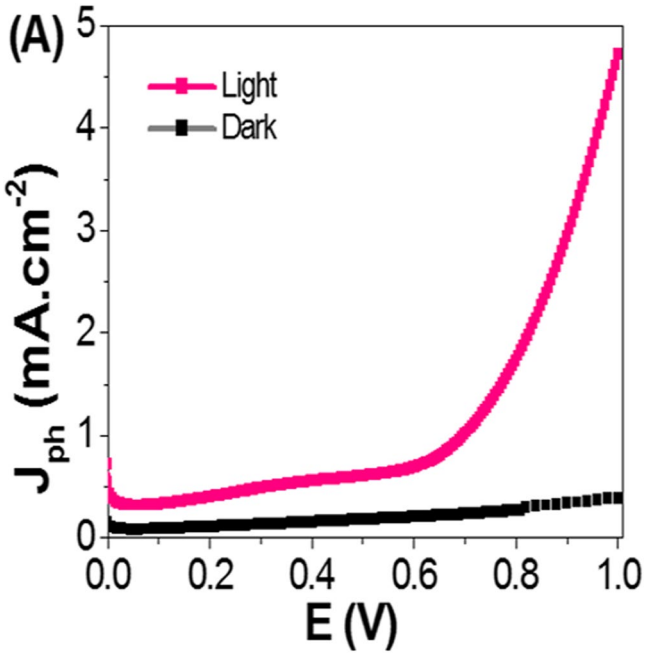

Figure 5. Photocurrent-voltage curves of PANI/PbS/ITO membrane electrode under illumination of 400 W metal-halide Lamp (**A**) without the optical filter in dark and light and (**B**) with optical filters of different wavelengths.

From Fig. 5, the current density-voltage (J_{ph}-E) behaviors of the PANI/PbS/ITO electrode is strongly affected by light exposure. The current densities are 0.4 and 4.76 mA.cm^{-2} in dark and light, respectively. In addition, the photocatalytic behavior of the nano/microcomposite membrane electrode is improved and the current density increased by increasing the applied voltage. Also, the values of the current density of the electrodes are firmly affected by the supporting ITO material that acts as a current collector.

PbS nanostructure acts as the main photocatalyst material in the PANI/PbS/ITO electrode for H_2 generation process, from which most of the photoelectrons produced[50]. To study the effect of PANI on the activity of PANI/PbS/ITO electrode for H_2 generation process, the photocurrent density-voltage (J_{ph}-E) curves of PANI/ITO electrode in the dark and artificial light illumination are measured and presented in Fig. 2S. From the figure, PANI/ITO electrode is slightly affected by light and acts as a photocathode, in which the values of the J_{ph} in dark and light at −1 V are −0.061 and −0.066 mA.cm^{-2}, respectively. PANI consists of mobile free electrons responsible for conductivity with asymmetry nature. Matveeva *et al.*[51] discussed the charge transfer behavior of PANI/ITO interface. The protonation of the ITO surface introduces some sort of charge exchange sites or current passes that reduce the additional barrier for charge transfer processes on the ITO/PANI interface and make easier charge transfer through them.

Figure 3S shows the variation of J_{ph} with the electric potential of the electrodes configurations under the illumination of monochromatic light. The optical filters of different wavelengths from 390 to 636 nm are used to control the wavelength of the illumination at 25 °C. From this figure, the J_{ph} values decrease with increasing of the wavelengths from 390 to 490 nm, with further increasing of the wavelengths, there are small changes in the values of J_{ph}. Then, the maximum J_{ph} values are obtained at wavelengths of 390 nm, which matched with the absorption peak positions (Fig. 4(A). Also, the distinct behavior of the photoanodes can be tentatively attributed to the enhanced solar absorption by the PANI/PbS core-shell nano/microcomposite that can cover a significant portion of the solar spectrum.

The stability of the PANI/PbS/ITO nano/microcomposite (II) membrane electrode is investigated for a prolonged time and shown in Fig. 6. During these experiments, a small bias voltage of 0.75 V is applied between the photoanode and the counter electrode to overcome any external losses of the measuring system. From Fig. 6, the J_{ph} values are decreased sharply from 4.76 to 1.4 mA.cm^{-2} as the time increased to 400 s. By further increasing the time to 2000 s, J_{ph} values almost remains constant due to the increasing accumulation of the ionic charges, which suggests a longer lifetime of the PANI/PbS/ITO nano/microcomposite electrode. Also, with increasing the time to 2000 s, the high density of surface states may lead to a significant pinning of the Fermi level that can facilitate the participation of these defect states in the surface oxidation process, leading to small degradation of the nano/microcomposite electrode[52].

The enhanced IPEC properties of the PANI/PbS/ITO nano/microcomposite membrane electrode is further confirmed by measuring the incident photon-to-current conversion efficiency (IPCE) under monochromatic illumination conditions as shown in Fig. 6(B). Such analytical measurements can also give a meaningful insight into the contribution of PANI/PbS nano/microcomposite in the conversion of the incident photons into charge carriers. The IPCE is determined at an applied potential of 1 V from Eq. (3)[53]:

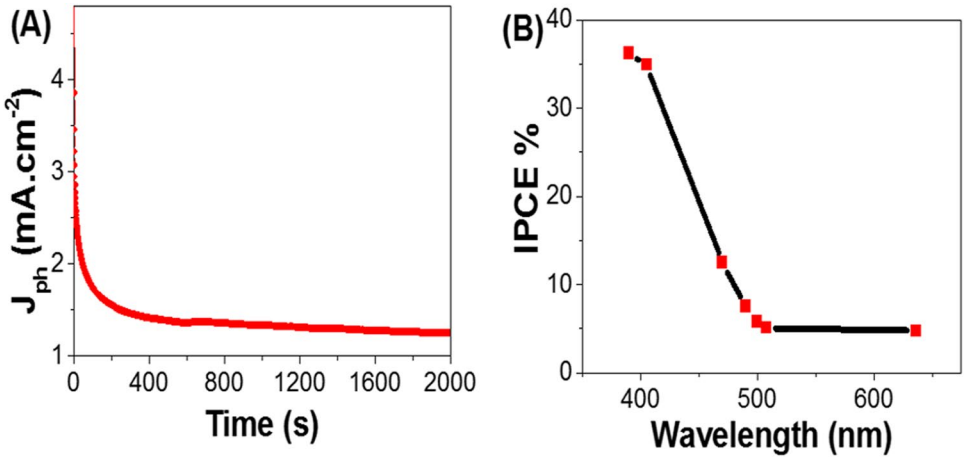

Figure 6. (**A**) current – time characteristic under illumination of 400 W metal-halide Lamp and (**B**) IPCE efficiency as a function of wavelength.

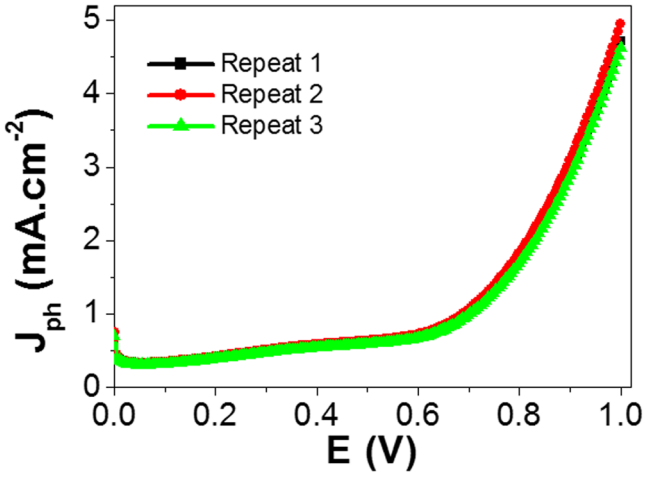

Figure 7. Reproducible studies of photocurrent density-voltage curves of PANI/PbS/ITO membrane electrodes under illumination of 400 W metal-halide Lamp without the optical filter.

$$\text{IPCE}(\%) = 1240.\frac{J_{ph}}{\lambda \,.\, \rho}.100 \tag{3}$$

where λ is the wavelength of the illuminating monochromatic photons and ρ is the illuminating light power density (mW.cm^{-2}). From Fig. 6(B), Based on the optical behavior of the nanocomposite, the optimum values for IPCE % are obtained at 390 and 405 nm with values of 36.5 and 35.2%, respectively. With increasing of the wavelengths, the IPCE % values decrease till reach 5% at 500 nm.

Form the experimental point of view; the reproducibility study is very important for confirming the obtained data[54]. Figure 7 shows the J_{ph} – E curves of the PANI/PbS/ITO electrode under illumination of 400 W metal-halide lamp without the optical filter for three repeats or cycles. Then, the statistical analyses are carried out depending on the reproducible studies of J_{ph} – E curves. From Fig. 7, the J_{ph} values for the PANI/PbS/ITO electrode are measured three times with Relative Standard Deviation (RSD) of 6.1% and a mean value of 4.78 mA.cm^{-2}.

Based on the previous experimental results for H_2 evolution using 0.3 M Na_2SO_3 solution as a sacrificing agent, the reaction mechanism is proposed in Fig. 8 for a better understanding of the photocatalytic process of PANI/PbS/ITO membrane photoanode. The surface electrons on ITO are transferred to the surface of the PANI nano/microparticles. Moreover, under the effect of artificial light, the levels of PANI are split, in which the electrons excitations take place. The transfer of electrons occurs from HOMO to LUMO levels[55]. Because of the existence of the potential difference between PANI and PbS levels, the LUMO electrons of PANI injected to the conducting band (CB) of PbS nanoparticle. Then, the PbS nanoparticles serve as electron donor material, in which the excited electrons can transfer from the core to out of the shell to H_2O because of electron tunneling process[56]. In the other side, the photogenerated holes on HOMO of PANI can migrate to PbS VB level. The $Na_2S_2O_3$ (sacrificing agent)

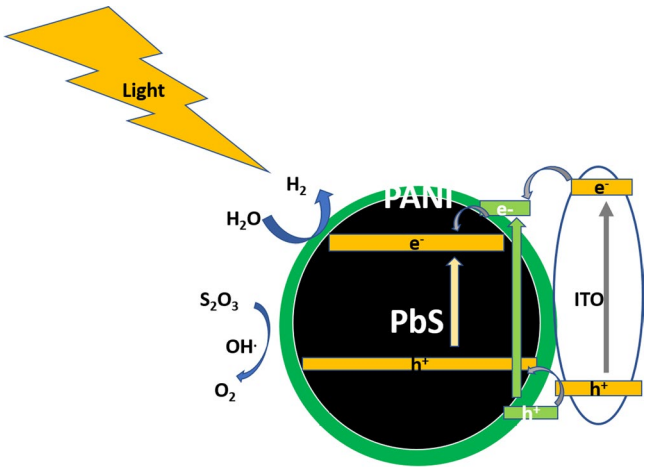

Figure 8. Mechanism of photochemical H_2 generation from H_2O using core-shell nano/microcomposite membrane electrode, PANI/PbS/ITO.

accept the holes from PbS for the O_2 evolution with the help of $OH^{\cdot}$ Radicals[55]. This electron-hole transition process is repeated with the lifetime of the prepared nanocomposite electrode that indicates a photocatalytic activity of the photocatalyst powder[57].

Conclusion

PbS nanoparticles were prepared by chemical bath deposition method at 80 °C, while, PANI nano/microparticles were prepared by the oxidative polymerization process. PANI/PbS core-shell nano/microcomposites (I, II, and III) were prepared by chemical polymerization of aniline in the presence of (0.05 g) PbS nanoparticles using aniline concentrations of 0.01, 0.03, and 0.05 M, respectively. The different concentrations of aniline were dissolved in 0.0005 M $H_2C_2O_4$ at 298 K. The chemical structures and morphologies of the prepared nano/micromaterials were determined using FT-IR, X-ray, SEM, and HR-TEM analyses. In addition, the optical absorbance analyses and bandgap calculations were carried out for all prepared nano/micromaterials. The core-shell nano/microcomposite (II) has the optimum optical data with strong absorption peak centered at 360 nm in the UV-region and another broad peak at 570 nm in the visible region. Moreover, it has the optimum bandgaps values of 1.41 and 2.79 eV. The core-shell nano/microcomposite (II) membrane electrode supported on ITO glass was applied as photoanode for H_2 electrogeneration from H_2O in the presence of $Na_2S_2O_3$. The H_2 electrogeneration took place using I-V characteristic behavior in the presence and absence of optical filters of different wavelengths at 298 K. Finally, IPCE under monochromatic illumination conditions were calculated. The optimum values for IPCE % were 36.5 and 35.2% that obtained at 390 and 405 nm, respectively.

Experimental Procedures

Preparation of PbS nanoparticles. The preparation process of PbS nanoparticles occurred by the chemical bath deposition method at 80 °C using the precursors $Pb(NO_3)_2$, thiourea, NaOH and Triethanolamine ($C_6H_{15}NO_3$) (Oxford Laboratory, India, 99%). In 100 ml beaker, 0.05 M $Pb(NO_3)_2$ (Oxford Laboratory, India, 99%), 0.04 M triethanolamine ($C_6H_{15}NO_3$) (Oxford Laboratory, India, 99%) and 0.2 M NaOH (El Nasr pharmaceutical company, Egypt, 99%) were dissolved well using the ultrasonic device for 30 min. The mixture then stirred at 80 °C for 15 min. After that, 0.06 M thiourea (Alpha chemical company, India, 99.1%) was added, and the mixture was further stirred for 15 min at the same temperature. The black precipitate was formed indicated the formation of PbS particles. Finally, the PbS particles were washed several times using warm distilled water and dried at 60 °C for 12 h.

Preparation of PANI nano/microparticles. PANI nano/microparticles were prepared by a sudden oxidative polymerization method. 0.03 M aniline (Rankem company, India, 99%) was dissolved in 0.0005 M $H_2C_2O_4$ (El Nasr pharmaceutical company, Egypt, 99%) under the effect of ultrasonic waves. By the same approach, 0.06 M $(NH_4)_2S_2O_8$ (Winlab company, UK, 98.5%) was dissolved well in 0.0005 M $H_2C_2O_4$. Moreover, the dissolved $(NH_4)_2S_2O_8$ was added over the dissolved aniline suddenly. In addition, the green precipitate was formed indication the polymerization of aniline to PANI (emeraldine salt). Then, the PANI was washed several times with warm water and dried at 60 °C for 12 h.

Preparation of PANI/PbS core-shell nano/microcomposites (I, II, and III). The prepared PbS nanoparticles were used as cores for the deposition of PANI shells by the oxidative polymerization process of aniline to form PANI/PbS core-shell nano/microcomposites. The oxidative polymerization was carried out using three different aniline concentrations; 0.01, 0.03, and 0.05 M, in which the nano/microcomposites are labeled as (I, II, and III), respectively. Aniline was dissolved in 20 ml (0.0005 M) $H_2C_2O_4$ at 298 K and then mixed with 0.05 g PbS nanoparticles. The polymerization process occurred using three different concentrations of $(NH_4)_2S_2O_8$ as an oxidant, such that the concentrations of oxidant to aniline in all solutions are 2:1. The three solutions were put

on ultrasonic for 1 h. After that, the samples were stirred for 5 h at 298 K using the magnetic stirrer device. The dark green precipitates (emeraldine salt) are formed indicating the completion of the polymerization process and formation of PANI/PbS core-shell nano/microcomposites (I, II, and III). Finally, the three nano/microcomposites (I, II, and III) are washed well with distilled H_2O and dried at 60 °C for 12 h.

Preparation of PANI/PbS core-shell nano/microcomposite (II) membrane electrode supported on ITO glass. PANI/PbS core-shell nano/microcomposite membrane electrode supported on ITO glass (Aldrich, 20 Ω) was prepared using the optimized optical analyses and applied for the photoelectrochemical H_2 generation. 3% of the nano/microcomposite (II) was mixed with 3% Dibutyl phthalate (DBP) (Middle-east company, Egypt, 99.5%) and 3% polyvinyl chloride (PVC) (Middle-east company, Egypt, 99.5%). All the components were mixed well and dissolved in minimum volume of Tetrahydrofuran (THF) (Middle-east company, Egypt, 99.5%). The resulting mixture was transferred into a Petri dish of 5 cm diameter. The total weight of constituents in each batch was fixed at 0.35 g. The Petri dish was then covered with a filter paper and left to dry in air. To obtain a uniform electrode thickness, the amount of THF was kept constant, and its evaporation was fixed for 24 h. The thickness of the electrode is ~0.2 mm. 10 mm diameter disk was cut out from the prepared electrode and glued to one side of ITO glass slide using Ag-THF paste.

Nano/microparticles characterization. The crystal structure of the deposited nano/microstructures PANI, PbS, and PANI/PbS were studied using high-resolution X-ray diffractometer system (model: PANalyticalX'Pert Pro, Holland) with CuK α radiation ($\lambda = 1.5406$ A°), operated at 45 kV and 40 mA. The XRD patterns were recorded in the 2θ range 10–90°. The pattern was analyzed by matching the observed peaks with the standard patterns provided by JCPDS files. Also, scanning analyses were carried out using Scanning Electron Microscope, SEM, (Model: ZEISS SUPRA 55 VP and ZEISS LEO, Gemini Column), and Transmission Electron Microscope, TEM, (JEOL JEM-2100 TEM). In addition, Fourier Transform Infrared Spectroscopy (FTIR) measurements were carried out using Shimadzu FTIR-340 Jasco spectrophotometer. Finally, the optical absorption spectra of the prepared PANI, PbS, and PANI/PbS nano/micromaterials were measured using Shimadzu UV spectrophotometer (M160 PC) at room temperature in the range 200–1100 nm.

Photoelectrochemical H_2 generation test. The photocatalytic hydrogen electro-generation experiments were performed by PANI/PbS core-shell nano/microcomposite (II) membrane electrode supported on ITO glass. The photoelectrochemical I-V and I-T behaviors were measured using Keithley measurement – source unit (2400 SourceMeter, A Tektronix company). Nano/microcomposite (II) membrane electrodes (1 cm^2) used as a working electrode, while Pt-electrode with the same dimensions was used as a counter electrode. 100 ml of 0.3 M $Na_2S_2O_3$ (El Nasr pharmaceutical company, Egypt, 99%) was used as the source electrolyte. The cell was exposed to an artificial light lamp (blended metal halide lamp 400 W, China) provided with series of linear optical filters.

References

1. Trevisan, R. *et al.* Harnessing infrared photons for photoelectrochemical hydrogen generation. A PbS quantum dot based "quasi-artificial leaf. *J Phys. Chem. Lett.* **4**, 141–146 (2012).
2. Walter, M. G. *et al.* Solar water splitting cells. *Chem Rev.* **110**, 6446–6473 (2010).
3. Van de Krol, R., Liang, Y. & Schoonman, J. Solar hydrogen production with nanostructured metal oxides. *J. Mater. Chem.* **18**, 2311–2320 (2008).
4. Fujishima, A. Electrochemical photolysis of water at a semiconductor electrode. *nature* **238**, 37–38 (1972).
5. Liu, S., Zhang, N. & Xu, Y. J. Core–shell structured nanocomposites for photocatalytic selective organic transformations. *Part. Part. Syst. Char.* **31**, 540–556 (2014).
6. Yang, G., Yan, W., Zhang, Q., Shen, S. & Ding, S. One-dimensional CdS/ZnO core/shell nanofibers via single-spinneret electrospinning: tunable morphology and efficient photocatalytic hydrogen production. *Nanoscale* **5**, 12432–12439 (2013).
7. Ellingson, R. J. *et al.* Highly efficient multiple exciton generation in colloidal PbSe and PbS quantum dots. *Nano lett.* **5**, 865–871 (2005).
8. Yu, L. *et al.* A generally synthetic route to semiconducting metal sulfide nanocrystals by using corresponding metal powder and cysteine as metallic and sulfuric sources, respectively. *Inorg. Chim. Acta* **376**, 659–663 (2011).
9. Ji, W. *et al.* High color purity ZnSe/ZnS core/shell quantum dot based blue light emitting diodes with an inverted device structure. *Appl Phys Lett.* **103**, 053106 (2013).
10. Lee, S. M. & Cho, Y. S. Characteristics of $Cu_2ZnSnSe4$ and $Cu_2ZnSn(Se, S)_4$ absorber thin films prepared by post selenization and sequential sulfurization of co-evaporated Cu–Zn–Sn precursors. *J.Alloy Compd.* **579**, 279–283 (2013).
11. Yeon, D. H., Lee, S. M., Jo, Y. H., Moon, J. & Cho, Y. S. Origin of the enhanced photovoltaic characteristics of PbS thin film solar cells processed at near room temperature. *J.Mater. Chem. A* **2**, 20112–20117 (2014).
12. Mohamed, H., Abdel-Hafiez, M., Miroshnikov, B., Barinov, A. & Miroshnikova, I. Spectral characteristics and morphology of nanostructured Pb–S–O thin films synthesized via two different methods. *Mat. Sci. Semicon. Proc.* **27**, 725–732 (2014).
13. Law, M. *et al.* Determining the internal quantum efficiency of PbSe nanocrystal solar cells with the aid of an optical model. *Nano lett.* **8**, 3904–3910 (2008).
14. Wu, J., Tang, C., Xu, H. & Yan, W. Enhanced photoelectrochemical performance of PbS sensitized Sb-SnO_2/TiO_2 nanotube arrays electrode under visible light illumination. *J.Alloy.Compd.* **633**, 83–91 (2015).
15. Niitsoo, O. *et al.* Chemical bath deposited CdS/CdSe-sensitized porous TiO_2 solar cells. *J. Photoch. Photobio A* **181**, 306–313 (2006).
16. Hsu, C.-H., Chen, C.-H. & Chen, D.-H. Decoration of PbS nanoparticles on Al-doped ZnO nanorod array thin film with hydrogen treatment as a photoelectrode for solar water splitting. *J.Alloy. Compd.* **554**, 45–50 (2013).
17. Hernandez-Borja, J., Vorobiev, Y. V. & Ramirez-Bon, R. Thin film solar cells of CdS/PbS chemically deposited by anammoniafree process. Sol. *Energ Mat. Sol. C* **95**, 1882–1888 (2011).
18. Cui, W. *et al.* Synthesis of PbS–$K_2La_2Ti_3O_{10}$ composite and its photocatalytic activity for hydrogen production. *Prog. Nat.Sci.* **22**, 120–125 (2012).
19. Chaudhuri, G. R. & Paria, S. Core/shell nanoparticles: classes, properties, synthesis mechanisms, characterization, and applications. *Chem Rev.* **112**, 2373–2433 (2011).

20. Lu, X., Zhang, W., Wang, C., Wen, T.-C. & Wei, Y. One-dimensional conducting polymer nanocomposites: synthesis, properties and applications. *Prog.Polym. Sci.* **36**, 671–712 (2011).
21. Tran, H. D., Li, D. & Kaner, R. B. One-dimensional conducting polymer nanostructures: bulk synthesis and applications. *Adv. Mat.* **21**, 1487–1499 (2009).
22. Karim, M. R. *et al*. Conducting polyaniline-titanium dioxide nanocomposites prepared by inverted emulsion polymerization. *Polym.Composite* **31**, 83–88 (2010).
23. Shang, M. *et al*. Efficient visible light-induced photocatalytic degradation of contaminant by spindle-like PANI/$BiVO_4$. *J.Phys.Chem. C* **113**, 20228–20233 (2009).
24. Li, X. *et al*. Preparation of polyaniline-modified TiO_2 nanoparticles and their photocatalytic activity under visible light illumination. *Appl.Catal. B Environ.* **81**, 267–273 (2008).
25. Geng, L. *et al*. Characterization and gas sensitivity study of polyaniline/SnO_2 hybrid material prepared by hydrothermal route. *Sensor Actuat. B Chem.* **120**, 568–572 (2007).
26. Wei, X., Jiao, L., Sun, J., Liu, S. & Yuan, H. Synthesis, electrochemical, and gas sensitivity performance of polyaniline/MoO_3 hybrid materials. *J. Solid State Electr.* **14**, 197–202 (2010).
27. Wang, C. *et al*. Probing effective photocorrosion inhibition and highly improved photocatalytic hydrogen production on monodisperse PANI@CdS core-shell nanospheres. *Appl. Catal. B: Environ.* **188**, 351–359 (2016).
28. Zhang, S., Chen, Q., Jing, D., Wang, Y. & Guo, L. Visible photoactivity and antiphotocorrosion performance of PdS–CdS photocatalysts modified by polyaniline. *Int. J. hydrogen energy* **37**, 791–796 (2012).
29. Guo, Y. *et al*. Enhancement of visible-light photocatalytic activity of Pt supported potassium niobate (Pt-$KNbO_3$) by up-conversion luminescence agent (Er^{3+}:$Y_3Al_5O_{12}$) for hydrogen evolution from aqueous methanol Solution. *Energy* **82**, 1–8 (2015).
30. Oz, Ç., Cos, B., Filiz, K. & Figen, A. K. The effect of vinegar-acetic acid solution on the hydrogen generation performance of mechanochemically modified Magnesium (Mg) granules. *Energy* **127**, 328–334 (2017).
31. Lin, Y. *et al*. Semiconductor nanostructure-based photoelectrochemical water splitting: A brief review. *Chem Phys Lett.* **507**, 209–215 (2011).
32. Yang, S., Prendergast, D. & Neaton, J. B. Tuning semiconductor band edge energies for solar photocatalysis via surface ligand passivation. *Nano lett.* **12**, 383–388 (2011).
33. Thimsen, E., Le Formal, F., Grätzel, M. & Warren, S. C. Influence of plasmonic Au nanoparticles on the photoactivity of Fe_2O_3 electrodes for water splitting. *Nano lett.* **11**, 35–43 (2010).
34. Chen, H. M. *et al*. Quantum dot monolayer sensitized ZnO nanowire-array photoelectrodes: true efficiency for water splitting. *Angew. Chem.* **122**, 6102–6105 (2010).
35. Khmissi, H., El Sayed, A. & Shaban, M. Structural, morphological, optical properties and wettability of spin-coated copper oxide; influences of film thickness, Ni, and (La, Ni) co-doping. *J.Mater. Sci.* **51**, 5924–5938 (2016).
36. Wu, T. M., Lin, Y. W. & Liao, C. S. Preparation and characterization of polyaniline/multi-walled carbon nanotube composites. *Carbon* **43**, 734–740 (2005).
37. Li, Y. *et al*. Enhanced electrochemical performance of polyaniline/sulfonated polyhedral oligosilsesquioxane nanocomposites with porous and ordered hierarchical nanostructure. *J. Mater. Chem.* **22**, 1884–1892 (2012).
38. Lin, W. *et al*. Hierarchical porous polyaniline–silsesquioxane conjugated hybrids with enhanced electrochemical capacitance. *RSC Adv.* **4**, 39508–39518 (2014).
39. Sayyah, S., Shaban, M. & Rabia, M. Electropolymerization of m-Toluidin on Platinum Electrode from Aqueous Acidic Solution and Character of the Obtained Polymer. *Adv. Polym. Tech.* **99**, 1–9 (2016).
40. Masid Roy, S., Rao, N. N., Herissan, A. & Colbeau-Justin, C. Polyaniline film-based wireless photo reactor for hydrogen generation through exciton mediated proton reduction. *Polymer* **112**, 351–358 (2017).
41. Li, C., Ahmed, T., Mab, M., Edvinsson, T. & Zhu, J. A facile, approach to ZnO/CdS nanoarrays and their photocatalytic and photoelectrochemical properties. *Appl Catal B Environ.* **175**, 38–139 (2013).
42. Braiek, Z. *et al*. Impact of In_2S_3 shells thickness on the electrochemical and optical properties of oriented ZnO/In_2S_3 core/shell nanowires. *Int. J. hydrogen energy* **42**, 5694–5707 (2017).
43. Sayyah, S. M., Shaban, M. & Rabia, M. A sensor of m-toluidine/m-cresol polymer film for detection of lead ions by potentiometric method. *Sensor Lett.* **13**, 961–966 (2015).
44. Shi, X. *et al*. Multiple exciton generation application of PbS quantum dots in ZnO@PbS/graphene oxide for enhanced photocatalytic activity. *Appl. Catal. B. Envir.* **163**, 123–128 (2015).
45. Zhang, X. *et al*. Reduced graphene oxide and PbS nanoparticles co-modified TiO_2 nanotube arrays as a recyclable and stable photocatalyst for efficient degradation of pentachlorophenol. *Appl. Catal. A Gen.* **457**, 78–84 (2013).
46. Garnier, F., Mullen, K. & Wegner, G. Electronic Materials: The Oligomer Approach, 1st edn (Wiley-VCH: Weinheim; 1998).
47. Shaban, M, *et al*. Preparation and characterization of polyaniline and Ag/polyaniline composite nanoporous particles and their antimicrobial activities. *J Polym Environ*., 1–9, https://doi.org/10.1007/s10924-017-0937-1 (2017).
48. Khedr, M. H., Fargali, A. A., El Rouby, W. M. A. & Hamdedein, A. A. Properties of pure and (Gd, Sm) doped CeO_2 nano-particles. *Int. J. Adv. Res.* **3**, 866–872 (2015).
49. Umrao, S. *et al*. A possible mechanism for the emergence of an additional band gap due to a Ti O C bond in the TiO_2–graphene hybrid system for enhanced photodegradation of methylene blue under visible light. *RSC Adv.* **4**, 59890–59901 (2014).
50. Shia, X. *et al*. Multiple exciton generation application of PbS quantum dots in ZnO@PbS/graphene oxide for enhanced photocatalytic activity. *Appl. Catal. B. Envir.* **163**, 123–128 (2015).
51. Matveeva, E. S., Gimenez, C. F. & Tejera, M. J. G. Charge transfer behavior of the indium–tin oxide/polyaniline interface: dependence on pH and redox state of PANI. *Synthetic Met.* **123**, 117–123 (2001).
52. Liua, Y. *et al*. Cactus-like hierarchical nanorod-nanosheet mixed dimensional photoanode for efficient and stable water splitting. *Nano Energy* **35**, 189–198 (2017).
53. Luo, Z., Li, C., Liu, S., Wang, T. & Gong, J. Gradient doping of phosphorus in Fe_2O_3 nanoarray photoanodes for enhanced charge separation. *Chem. Sci.* **8**, 91–100 (2017).
54. Sayyah, S. M., Shaban, M. & Rabia, M. A high-sensitivity potentiometric mercuric ion sensor based on m-toluidine films. *IEEE Sensor J* **6**, 1541–1548 (2016).
55. Xu, H. *et al*. Fabrication of polyaniline sensitized grey-TiO_2 nanocomposites and enhanced photocatalytic activity. *Sep. Purif. Tech.* **184**, 248–256 (2017).
56. Huang, L. *et al*. Dual cocatalysts loaded type I CdS/ZnS core/shell nanocrystals as effective and stable photocatalysts for H_2 evolution. *J Phys Chem C* **117**, 11584–11591 (2012).
57. Kisch, H. & Bahnemann, D. Best Practice in Photocatalysis: Comparing Rates or Apparent Quantum Yields. *J. Phys. Chem. Lett.* **6**, 1907–1910 (2015).
58. Sayyah, S.M. Shaban, M. & Rabia, M. Electropolymerization kinetics, characterization and application: (Polymer/Pt)-electrode as pH and heavy metal sensors, 1st edn (Lambert Academic Publishing, Germany, 2016).
59. Ismail, N. S. M., Ramli, N., Hani, N. M. & Meon, Z. Extraction and characterization of pectin from dragon fruit (Hylocereus polyrhizus) using various extraction conditions.(Pengekstrakan dan pencirian pektin daripada buah naga (hylocereus polyrhizus) menggunakan pelbagai keadaan pengekstrakan. *Sains Malaysiana* **41**, 41–45 (2012).

60. Borhade, A. & Uphade, B. A. comparative study on characterization and photocatalytic activities of PbS and Co doped PbS nanoparticles. *Chalcogenide Lett.* **9**, 299–306 (2012).
61. Sayyah, S., Shaban, M. & Rabia, M. m-Toluidine polymer film coated platinum electrode as a pH sensor by potentiometric methods. *Sensor lett.* **13**, 961–966 (2015).

Author Contributions

M. Rabia, H. S. H. Mohamed, and M. Shaban designed the experiments, characterized the samples, and contributed to the writing of the manuscript, S. Taha analyzed some data and contributed to the experimental part.

Additional Information

Supplementary information accompanies this paper at https://doi.org/10.1038/s41598-018-19326-w.

Competing Interests: The authors declare that they have no competing interests.

Publisher's note: Springer Nature remains neutral with regard to jurisdictional claims in published maps and institutional affiliations.